Nanoscale

RSC Publishing

PAPER

View Article Online
View Journal | View Issue

Cite this: *Nanoscale*, 2013, **5**, 8375

Photocatalytic water splitting for hydrogen generation on cubic, orthorhombic, and tetragonal $KNbO_3$ microcubes†

Tingting Zhang,[ac] Kun Zhao,[a] Jiaguo Yu,[d] Jian Jin,[d] Yang Qi,[c] Huiquan Li,[b] Xinjuan Hou*[b] and Gang Liu*[a]

Potassium niobate ($KNbO_3$) microcubes with orthorhombic and tetragonal phases were hydrothermally prepared and characterized by powder X-ray diffraction, nitrogen adsorption–desorption, micro-Raman spectroscopy, Fourier transform infrared spectroscopy, diffuse reflectance UV-visible spectroscopy, X-ray photoelectron spectroscopy, scanning electron microscopy, and high-resolution transmission electron microscopy. The photoreactivity of the as-prepared $KNbO_3$ samples was evaluated regarding the hydrogen evolution from aqueous methanol under UV, and the results were compared with that of cubic $KNbO_3$ microcubes. The photocatalytic reactivity was shown to be phase-dependent, following the order cubic > orthorhombic > tetragonal. Insight into the phase-dependent photocatalytic properties was gained by first-principles density functional calculations. The best photocatalytic performance of cubic $KNbO_3$ is ascribed to it having the highest symmetry in the bulk structure and associated unique electronic structure. Further, the surface electronic structure plays a key role leading to the discrepancy in photoreactivity between orthorhombic and tetragonal $KNbO_3$. The results from this study are potentially applicable to a range of perovskite-type mixed metal oxides useful in water splitting as well as other areas of heterogeneous photocatalysis.

Received 8th May 2013
Accepted 23rd May 2013

DOI: 10.1039/c3nr02356g

www.rsc.org/nanoscale

1 Introduction

Fossil fuels are non-renewable energy sources and their combustion has caused a series of global environmental concerns such as climate change and ocean acidification. From the view points of energy and environmentally sustainable development, using clean, abundant and sustainable energy without fossil fuel consumption and CO_2 emission is of great significance. Owing to its high combustion energy and zero emission, hydrogen has been identified as an ideal alternative to fossil fuels. Currently, hydrogen is mainly produced by reforming petroleum and natural gas at high temperature. In 1972, Fujishima and Honda discovered that semiconductor TiO_2 electrodes can split water into hydrogen under light illumination at room temperature.[1] For the past decades, significant attention has been directed toward heterogeneous photocatalysis, aiming to convert renewables into hydrogen.[2–11] Among a diverse set of novel photocatalysts, perovskite-type mixed metal oxides (general formula ABO_3, where A is a metal, B is a second metal, and O is oxygen), such as $SrTiO_3$,[12] $NaTaO_3$,[13] and $AgNbO_3$,[14] are attractive due to their availability and low toxicity. Because the conduction band (CB) edge of perovskite oxides is often more negative than the H^+/H_2 energy level, they can split water without any external bias potential.[15] Known to be highly stable under light illumination and nontoxic, potassium niobate ($KNbO_3$) has been studied in photocatalytic water splitting for hydrogen production.[16,17] In general, $KNbO_3$ presents a number of temperature-dependent crystalline phases, such as orthorhombic, tetragonal and cubic. Those crystalline phases with various inherent bulk crystal structures are based on a perovskite unit. In the case of hydrogen generation photocatalyzed by $KNbO_3$, most studies were carried out in the orthorhombic phase.[16,17]

In order to optimize the photocatalytic efficiency and provide a sufficient base for future design and development of high-performance photocatalysts, great efforts have been made to probe the underlying principles and photocatalytic materials. In this regard, engineering of nano- and microcrystalline photocatalysts in terms of their structure and morphology is one of the approaches enabling highly efficient water splitting. For

[a]*National Center for Nanoscience and Technology, Beijing 100190, China. E-mail: liug@nanoctr.cn; Fax: +86-10-62656765; Tel: +86-10-82545613*

[b]*National Engineering Laboratory for Hydrometallurgical Cleaner Production Technology, Institute of Process Engineering, Chinese Academy of Sciences, Beijing, 100190, China. E-mail: xjhou@home.ipe.ac.cn; Fax: +86-10-82544830; Tel: +86-10-82544830*

[c]*Institute of Materials Physics and Chemistry, School of Sciences, Northeastern University, Shenyang 110004, China*

[d]*State Key Laboratory of Advance Technology for Material Synthesis and Processing, Wuhan University of Technology, Wuhan 430070, China*

† Electronic supplementary information (ESI) available. See DOI: 10.1039/c3nr02356g

instance, morphology,[18] exposed facets[19–21] and crystalline phase[22–25] were found to play an indispensable role in affecting the observed photocatalytic properties. To date, most studies have been focused on TiO_2,[26–30] and much less information is available on other types of photocatalysts, including alkaline niobates. It is evident that our current understanding of the structure–reactivity relationship in photocatalytic water splitting is inadequate. In particular, systematic exploration of crystalline phase-mediated photocatalytic H_2 generation is still lacking, albeit the crystalline phase is a crucial parameter.[30,31] Only a fundamental understanding of relevant principles and photocatalytic materials at the atomic level will guide the design and tailoring of efficient photocatalysts. Herein, we hydrothermally synthesized orthorhombic and tetragonal micro-sized $KNbO_3$ cubes. Further, we examined their photocatalytic properties regarding hydrogen generation by water splitting, and the results were compared with that of cubic $KNbO_3$ in the form of microcubes. For the first time, first-principles density functional calculations were performed to provide insights into the origin of the underlying mechanism governing the photocatalytic performance of cubic, orthorhombic and tetragonal $KNbO_3$ with cube-like morphology.

2 Experimental section

2.1 Synthesis

Tetragonal $KNbO_3$ microcubes (denoted as t-$KNbO_3$ MCs) were hydrothermally synthesized using a method adapted from prior work.[32] First, 20 g potassium hydroxide and potassium carbonate (KOH, 85% min., K_2CO_3 2.0% max., Alfa Aesar) were dissolved into 14 mL Milli-Q water (18 MΩ cm, Millipore) with magnetic stirring. After being completely dissolved, 1.89 g niobium oxide (Nb_2O_5, puratronic 99.9985%, Alfa Aesar) was added slowly to that solution. Next, the mixture was stirred vigorously at room temperature for 30 min. Then it was transformed into a Teflon-lined autoclave (50 mL) and heated in an oil bath at 180 °C for 12 h. A white precipitate was collected and washed several times with Milli-Q water (18 MΩ cm, Millipore) and ethanol, then dried at 60 °C for 12 h. Orthorhombic $KNbO_3$ microcubes (denoted as o-$KNbO_3$ MCs) were obtained using almost the same recipe as t-$KNbO_3$. The only difference was the amounts of KOH and Nb_2O_5, which were 22.6 and 2.5 g, respectively.

2.2 Characterization

The crystal structures of the as-prepared samples were investigated with a Shimadzu X-ray diffractometer (XRD-6000) using a Cu Kα radiation (50 kV, 300 mA) source ($\lambda = 0.154178$ nm) at a scanning rate of 10 ° min^{-1} in the 2θ range of 10–85°. The Raman spectra were measured on a Renishaw Micro-Raman Spectroscopy System (Renishaw in Via plus) using a Renishaw 514 nm laser. Fourier transform infrared (FTIR) spectra were obtained between 4000 and 400 cm^{-1} with sixteen scans and a resolution of 4 cm^{-1} on a Perkin Elmer Spectrum 9000, using wafers containing KBr and $KNbO_3$ mixed powders. Diffuse reflectance ultraviolet and visible (DRUV-vis) spectra were recorded at room temperature in the range of 200–800 nm using a Perkin Elmer Lambda 950 UV-vis spectrometer. Fine $BaSO_4$ powders were used as a standard. The Brunauer–Emmett–Teller (BET) specific surface area was measured using a Micromeritics ASAP 2020 apparatus. X-ray photoelectron spectroscopy (XPS) data were obtained by using an ESCALab 250 Xi electron spectrometer from Thermo Scientific Corporation. For high-resolution measurements, a 150 W monochromatic Al Kα source with a pass energy of 30 eV was employed. Low-energy electrons were used for charge compensation. The peak positions were internally referenced to the adventitious C 1s line at 284.8 eV. The morphology of the as-synthesized samples was characterized by a Hitachi S-4800 field emission scanning electron microscope (SEM). High-resolution transmission electron microscopy (TEM) images were collected with Tecnai G2 F20UT and G2 20ST microscopes operating at an accelerating voltage of 200 kV.

2.3 Photocatalytic hydrogen evolution

Photocatalytic measurements were carried out in a 300 mL pyrex reactor and an on-line gas chromatograph (Tianmei GC-7900) equipped with a thermal conductivity detector. 100 mg of the photocatalyst were suspended in a 25% methanol aqueous solution (20 mL methanol + 60 mL distilled water) under magnetic stirring. Platinum (Pt) as a co-catalyst was deposited onto the $KNbO_3$ samples from a $H_2PtCl_6 \cdot 6H_2O$ aqueous solution *via in situ* photodeposition. Subsequently, the suspensions were purged with a vacuum pump before light irradiation in order to remove the dissolved air. A 300 W xenon arc lamp with a wavelength range of 250–380 nm was positioned *ca.* 17.5 cm away from the reactor and the hydrogen evolution was monitored quantitatively by on-line GC.

The apparent quantum efficiency (QE) was measured using four 3 W LEDs ($\lambda = 365$ nm) positioned about 1 cm away from the reactor in four directions. The QE (%) was calculated based on the following equation:

$$\mathrm{QE}\ (\%) = N_e/N_p = 2N_{H_2}/N_p \quad (1)$$

where N_e is the number of reacted electrons, N_p is the number of incident photons, and N_{H_2} is the number of evolved H_2 molecules.

2.4 Theoretical calculations

Plane-wave density functional theory (DFT) calculations with the CASTEP program package[33] were performed to obtain the band structures, densities of state (DOS), and partial densities of state (PDOS) of cubic, orthorhombic and tetragonal $KNbO_3$. The generalized gradient approximation (GGA) with the Perdew–Burke–Ernzerh (PBE) function was adopted for the exchange–correction potential. The projector augmented wave potentials and the cut energy of 380 eV were used with the core electrons replaced by ultrasoft pseudopotentials. Both the atomic positions and the unit cell were allowed to relax simultaneously within the symmetry constraints imposed by the $Pm\bar{3}m$, $Amm2$ and $P4mm$ space groups for cubic, orthorhombic and tetragonal $KNbO_3$, respectively. The respective k-point sets

of 4 × 2 × 2, 4 × 3 × 2 and 4 × 4 × 3 were used for c-$KNbO_3$, o-$KNbO_3$ and t-$KNbO_3$. Based on the optimized bulk crystal structure, the corresponding surface models for (110) and (001) of o-$KNbO_3$, (100) and (001) of t-$KNbO_3$ were cleaved, and a vacuum layer of 1.5 nm was added.

3 Results and discussion

3.1 Sample characterization

Fig. 1 illustrates the crystal structures of cubic, orthorhombic and tetragonal $KNbO_3$. It is well established that the ideal perovskite-type structure is cubic with the space group $Pm\bar{3}m$.[15] The orthorhombic and tetragonal structures are isostructural to the perovskite-type, having structural distortion with respect to the cubic structure.[15] Fig. S1† displays the XRD patterns in the JCPDS database card for orthorhombic (32-0822) and tetragonal (71-0945) $KNbO_3$. Fig. 2A(a) shows that the XRD peaks for o-$KNbO_3$ MCs are indexed to orthorhombic $KNbO_3$ (space group *Amm*2) with lattice constants of $a = 0.5695$, $b = 0.5721$, and $c = 0.3973$ nm (JCPDS card 32-0822). The XRD peaks shown in Fig. 2A(b) for t-$KNbO_3$ MCs are indexed to tetragonal $KNbO_3$ (space group *P*4*mm*) with lattice constants of $a = 0.3996$, $b = 0.3996$, and $c = 0.4063$ nm (JCPDS card 71-0945). Panel B in Fig. 2 displays that there exists a distinct difference between tetragonal and orthorhombic $KNbO_3$ at *ca.* 45°. In the case of orthorhombic $KNbO_3$, two diffraction peaks located at 45.0° and 45.5° are indexed to (220) and (002). For tetragonal $KNbO_3$, two peaks located at 44.8° and 45.3° are well resolved and indexed to (002) and (200), respectively.[32] Moreover, XRD patterns at *ca.* 22.0° and 31.5° are given in Fig. S2† aiming to show additional differences between o-$KNbO_3$ and t-$KNbO_3$. The XRD patterns strongly suggest that the orthorhombic and tetragonal $KNbO_3$ were synthesized successfully. Fig. 3 shows the corresponding micro-Raman spectra of the as-synthesized $KNbO_3$ samples. The major bands of o-$KNbO_3$ MCs are in good agreement with that of $KNbO_3$ reported in our previous work.[34] It is notable that in the range of 165–235 cm^{-1}, o-$KNbO_3$ MCs and t-$KNbO_3$ MCs present minor differences. For instance, the band located at 191 cm^{-1} for o-$KNbO_3$ MCs shifts to a higher wavenumber (red-shift) by 2 cm^{-1} relative to t-$KNbO_3$ MCs. The bands can be attributed to the internal vibrational modes of the NbO_6 octahedron. ν_1 (592 cm^{-1}) and ν_2 (532 cm^{-1}) are two stretching modes, and ν_5 (280 cm^{-1}) is a bending mode. The weak band at 831 cm^{-1} corresponds to the combinational band of ν_1 and ν_5.[35] In general, Raman spectroscopy is more sensitive to lattice perturbations in the local structure in comparison to XRD. Such perturbations could reflect the variations of octahedral ligand fields, associated changes of Nb–O bond lengths and O–Nb–O bond angles, and play a key role in photocatalysis. It was reported that a metal–O bond length can be correlated to its Raman stretching frequency, with higher stretching frequencies reflecting the shorter metal–O bond lengths.[36] FTIR spectra of the as-prepared $KNbO_3$ samples are displayed in Fig. 4. Previous work showed absorption peaks in the range of 450–1000 cm^{-1}, which are attributed to the NbO_6 octahedron.[37] The broad, strong band centered at *ca.* 623 cm^{-1} represents the O–Nb–O stretching vibration (ν_3 mode) in the corner-shared NbO_6. The band around 500 cm^{-1} can be assigned to the edge-shared NbO_6 octahedron. Additionally, t-$KNbO_3$ has a relatively broad band at 500 cm^{-1}, suggesting that the crystalline structure of t-$KNbO_3$ is different from that of o-$KNbO_3$. It has been suggested that the edge-shared NbO_6 octahedron often exhibits larger structural distortions than the corner-shared NbO_6 octahedron and thus gives rise to variations in the Nb–O bond length.[15] The weak absorption bands at 3441 and 1641 cm^{-1} can be assigned to H_2O adsorbed on the surfaces of samples. The absorption band at 2853 cm^{-1} is referred to CH_2 symmetric stretching modes, and the band at 2921 cm^{-1} is ascribed to CH_3 symmetric stretching modes and CH_2 asymmetric stretching modes, probably due to some organic impurities such as compounds containing methyl and methylene groups in the KBr.[10] The bands at 2316, 2345 and 1383 cm^{-1} can be assigned to adsorbed CO_2 on the sample surfaces.

The electronic structure of the as-prepared samples was revealed by high-resolution XPS (Fig. 5). Fig. 5A shows that the binding energy for Nb $3d_{5/2}$ is *ca.* 206.4 and 206.5 eV for t-$KNbO_3$ MCs and o-$KNbO_3$ MCs, respectively. The observed difference in the Nb 3d binding energy indeed reflects the intrinsic bulk structure difference between tetragonal and orthorhombic $KNbO_3$, albeit the difference is very minor.[10,31] Fig. 5B displays the corresponding valence band (VB) spectra. Both o-$KNbO_3$ MCs and t-$KNbO_3$ MCs have a similar line shape in the VB. Using synchrotron-based XPS and X-ray emission spectroscopy (XES), Postnikov *et al.* studied the density of states (DOS) in the $KNbO_3$ VB and suggested that the top of the $KNbO_3$ VB is predominantly contributed by O 2p, and the bottom of the VB is contributed by Nb 4d.[38] Fig. 6A shows the DRUV-vis absorption spectra that were converted from the corresponding diffused reflectance spectra data based on the Kubelka–Munk function normalized at 250 nm. The band gap (E_g) can be estimated according to the following equation:

$$(\alpha h\nu)^n = A(h\nu - E_g) \quad (2)$$

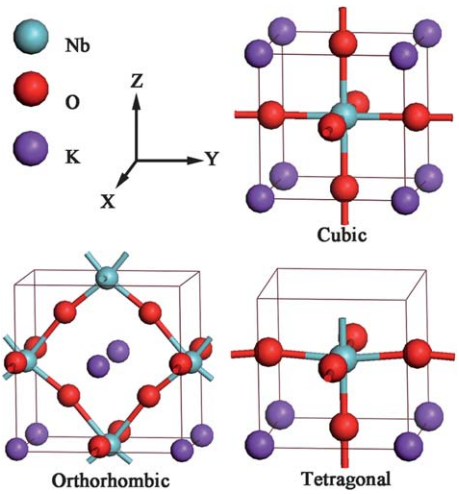

Fig. 1 Schematic crystal structures of cubic, orthorhombic and tetragonal $KNbO_3$. Cyan spheres are Nb, red spheres are oxygen and purple spheres are K.

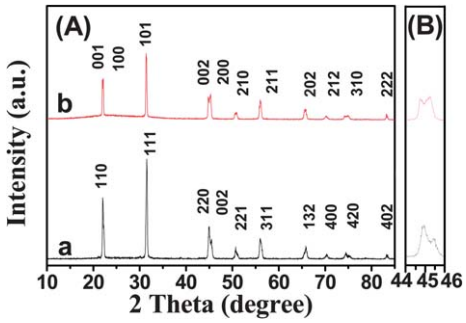

Fig. 2 (A) Powder XRD patterns of tetragonal and orthorhombic $KNbO_3$ samples. (B) Comparison of characteristic diffraction peaks between t-$KNbO_3$ and o-$KNbO_3$. (a) and (b) refer to o-$KNbO_3$ MCs and t-$KNbO_3$ MCs, respectively.

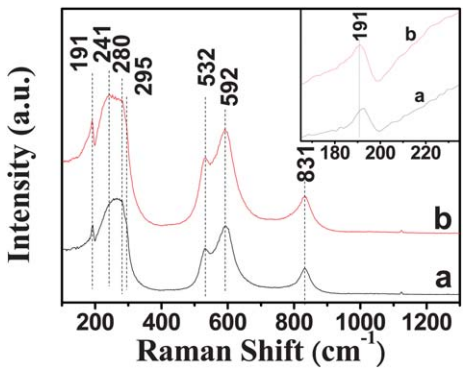

Fig. 3 Micro-Raman spectra of $KNbO_3$ samples. (a) and (b) refer to the respective o-$KNbO_3$ MCs and t-$KNbO_3$ MCs. The inset highlights the spectra in the range of 100–390 cm^{-1}.

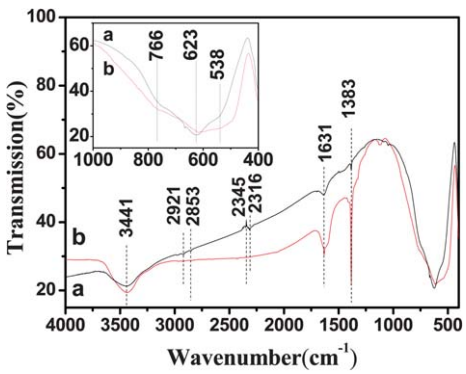

Fig. 4 FTIR spectra of $KNbO_3$ samples. (a) and (b) refer to o-$KNbO_3$ MCs and t-$KNbO_3$ MCs, respectively. The inset shows both spectra in the range of 1000–450 cm^{-1}.

where α, h, ν, A and E_g represent the respective absorption coefficient, Planck constant, light frequency, proportionality constant and band gap. It is generally accepted that the value of the index n is determined by the nature of the electronic transitions. Herein, n is 1/2 for an indirect band-gap semiconductor $KNbO_3$. Plotting $(\alpha h\nu)^{1/2}$ *versus* the photon energy ($h\nu$) as shown in Fig. 6B can estimate the E_g from the intercept of the tangent to the x-axis. E_g is 3.15 and 3.08 eV for o-$KNbO_3$ MCs and

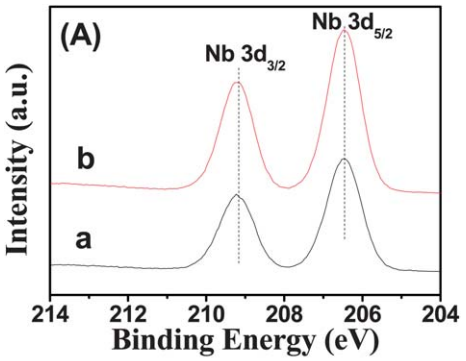

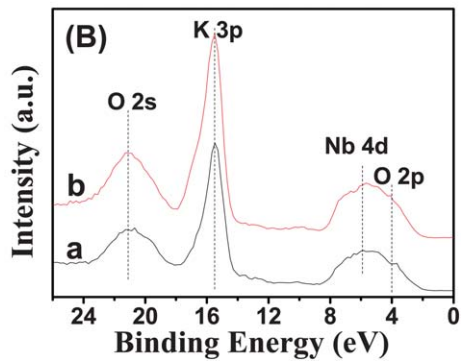

Fig. 5 (A) High-resolution XPS spectra of the Nb 3d core-level and (B) valence band for $KNbO_3$ samples; (a) and (b) refer to the respective o-$KNbO_3$ MCs and t-$KNbO_3$ MCs.

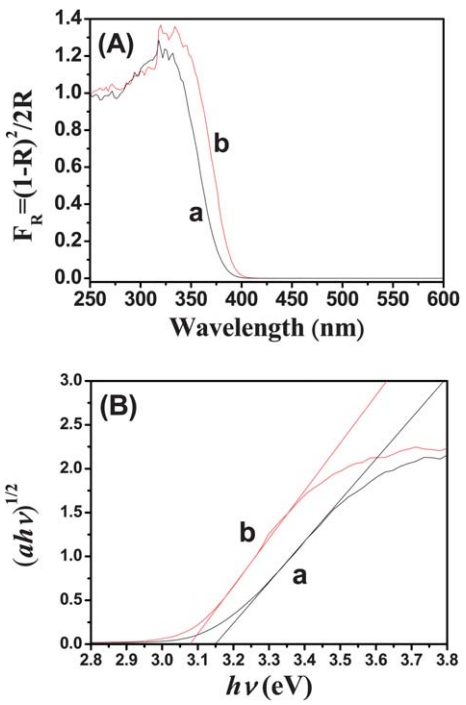

Fig. 6 (A) DRUV-vis spectra and (B) corresponding plots of $(\alpha h\nu)^{1/2}$ *versus* photon energy ($h\nu$) for o-$KNbO_3$ MCs and t-$KNbO_3$ MCs; (a) and (b) refer to o-$KNbO_3$ MCs and t-$KNbO_3$ MCs, respectively.

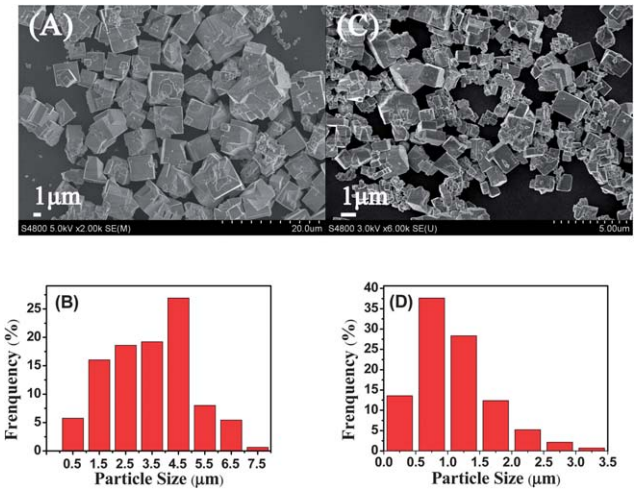

Fig. 7 Representative morphologies of the as-prepared $KNbO_3$ samples. (A) SEM image and (B) particle size distribution of t-$KNbO_3$ MCs. (C) SEM image and (D) particle size distribution of o-$KNbO_3$ MCs.

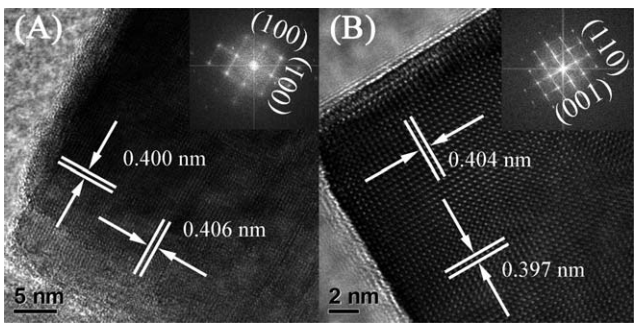

Fig. 8 High-resolution TEM image of the as-prepared $KNbO_3$ samples. Inset: FFT pattern. (A) HRTEM image of t-$KNbO_3$ MCs. (B) HRTEM image of o-$KNbO_3$ MCs.

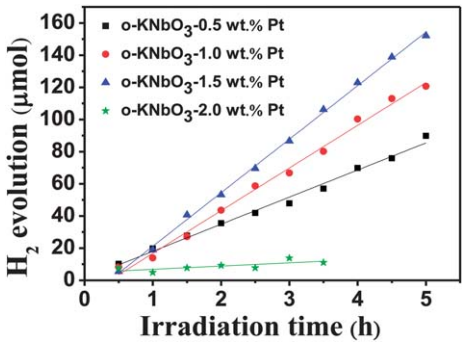

Fig. 9 Photocatalytic H_2 evolution from aqueous methanol over o-$KNbO_3$ MCs with 0.5, 1.0, 1.5 and 2.0 wt% Pt. *Reaction conditions*: 0.1 g catalyst, 25% methanol in aqueous solution (20 mL methanol + 60 mL distilled water), 300 W Xe-lamp (λ: 250–380 nm).

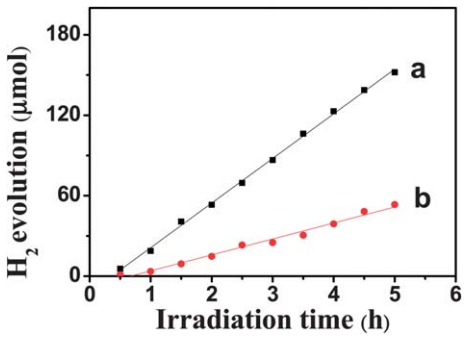

Fig. 10 Photocatalytic H_2 evolution from aqueous methanol over $KNbO_3$ samples with a loading of 1.5 wt% Pt; (a) and (b) refer to o-$KNbO_3$ MCs and t-$KNbO_3$ MCs, respectively. *Reaction conditions*: 0.1 g catalyst, 25% methanol in water (20 mL methanol + 60 mL distilled water), 300 W Xe-lamp (λ: 250–380 nm).

t-$KNbO_3$ MCs, respectively. The E_g values are close to that reported in prior studies, in which E_g was 3.14 (ref. 16) and 3.2 eV (ref. 17) for orthorhombic $KNbO_3$ in the form of nanorods and nanocubes, respectively. The difference in band gap is mainly due to the effects of the crystalline phase.[31]

The morphology of the as-prepared $KNbO_3$ samples was revealed by SEM. Although the synthesis method was adapted from previous work,[32] the as-obtained samples in the current work have a more uniform cube-like morphology. Fig. 7A and B show t-$KNbO_3$ microcubes and their particle size distribution. The average edge length is *ca.* 3.3 μm. In the case of o-$KNbO_3$ microcubes (Fig. 7C), the average edge length is *ca.* 1.0 μm (Fig. 7D). Fig. 8A presents the high-resolution TEM image and the corresponding FFT pattern (inset of Fig. 8A) of a t-$KNbO_3$ microcube. The lattice fringes are 0.406 and 0.400 nm, consistent with the respective (001) and (100) planes of t-$KNbO_3$. For o-$KNbO_3$ microcubes, the high-resolution TEM image (Fig. 8B) and corresponding FFT pattern (inset of Fig. 8B) indicate that the respective lattice fringes (0.404 and 0.397 nm) fit well to the (110) and (001) planes of o-$KNbO_3$.

The BET surface area was obtained from nitrogen adsorption–desorption isotherms and listed in Table 1. It is expected that both the crystalline phase[31] and exposed facets[39] of

Table 1 Physico-chemical properties of $KNbO_3$ samples

Samples	Size (μm)	BET surface area ($m^2\ g^{-1}$)	Band gap (eV)	Hydrogen production rate (μmol $h^{-1}\ g^{-1}$)	Normalized hydrogen production rate (μmol $h^{-1}\ m^{-1}$)	QE (%)
o-$KNbO_3$	1.0	1.42	3.15	333	234	0.53
t-$KNbO_3$	3.3	0.68	3.08	118	174	0.16
c-$KNbO_3$[a]	0.3	3.9	3.24	1242	318	1.95

[a] From ref. 10.

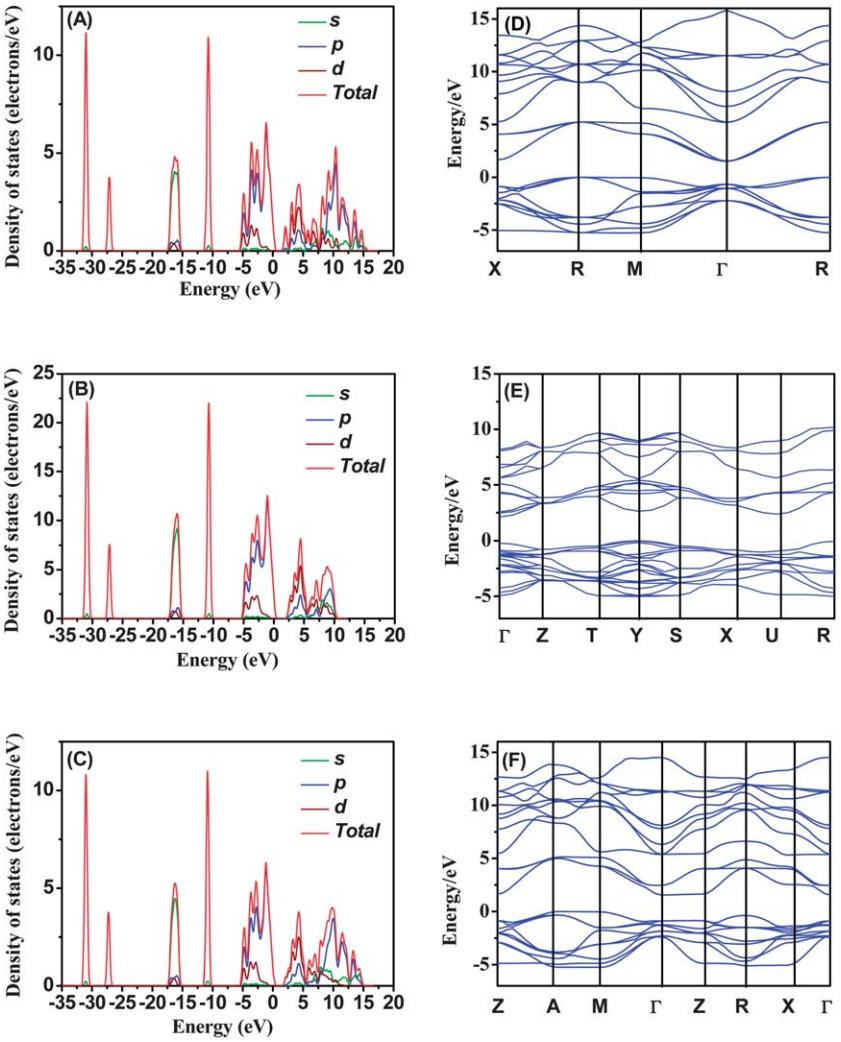

Fig. 11 The DOS of (A) c-$KNbO_3$ (B) o-$KNbO_3$ and (C) t-$KNbO_3$. The calculated band structures of (D) c-$KNbO_3$, (E) o-$KNbO_3$ and (F) t-$KNbO_3$.

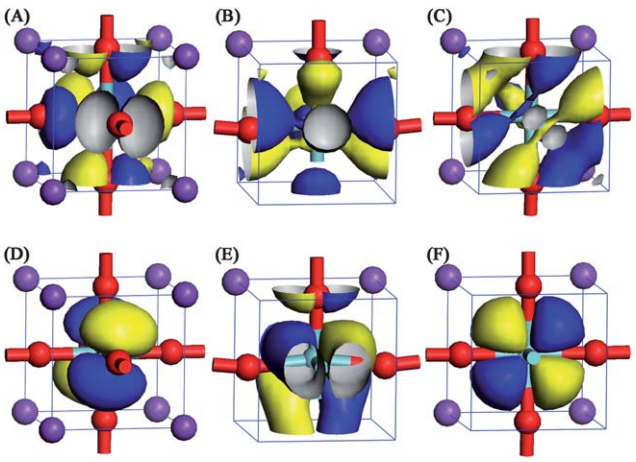

Fig. 12 Frontier orbital distributions of $KNbO_3$ for different crystalline phases. HOMO of (A) c-$KNbO_3$, (B) o-$KNbO_3$ and (C) t-$KNbO_3$. LUMO of (D) c-$KNbO_3$, (E) o-$KNbO_3$ and (F) t-$KNbO_3$. Cyan spheres are Nb, red spheres are oxygen and purple spheres are K.

photocatalysts probably influence photocatalytic water-splitting for hydrogen generation.

3.2 Photocatalytic activity for hydrogen evolution

The rate of photocatalytic water-splitting for hydrogen production was evaluated for o-$KNbO_3$ MCs and t-$KNbO_3$ MCs. A certain amount of Pt was deposited on the photocatalyst surface to act as a co-catalyst. In this case, the low H_2 overpotential on the Pt surface could facilitate H_2 generation. Further, under UV illumination, Pt serves as an electron trapping center that is rather effective in inhibiting charge recombination. Fig. 9 displays the photocatalytic H_2 evolution from aqueous methanol over o-$KNbO_3$ MCs as a function of Pt content under 300 W Xe-lamp illumination. The symbols are the experimental points and the solid line is obtained through the least-squares straight-line fitting. The H_2 evolution rate is 2.2, 16.8, 26.5 and 33.2 μmol h^{-1} for Pt loading of 2.0, 0.5, 1.0 and 1.5 wt%, respectively. o-$KNbO_3$ MCs with 1.5 wt% Pt display the highest H_2 evolution rate. Likewise, as shown in Fig. S3† t-$KNbO_3$ MCs with 1.5 wt% Pt also have the highest H_2 evolution rate. Thus, 1.5 wt% Pt was

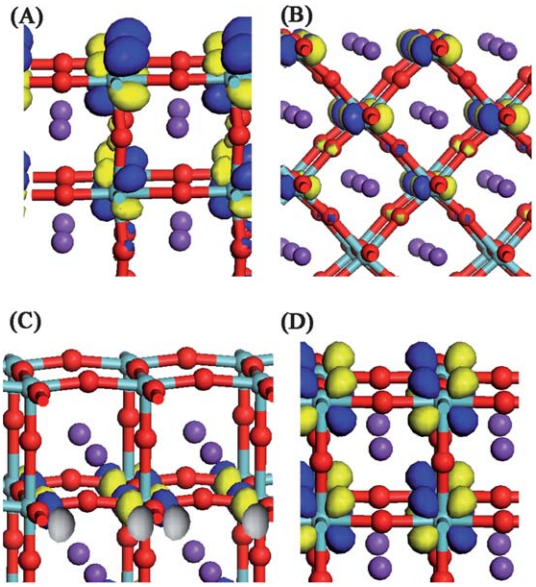

Fig. 13 Lowest unoccupied wave functions at (A) (001) and (B) (110) of o-$KNbO_3$, and the lowest unoccupied wave functions at (C) (001) and (D) (100) of t-$KNbO_3$. Cyan spheres are Nb, red spheres are oxygen and purple spheres are K.

used throughout our experiment. As displayed in Fig. 10, o-$KNbO_3$ MCs had a higher rate of hydrogen generation (332.8 μmol h^{-1} g^{-1}), which is approximately three times larger than that of t-$KNbO_3$ MCs (118.0 μmol h^{-1} g^{-1}). In order to probe the intrinsic difference of photocatalysis, the rate of hydrogen production was normalized with respect to the BET surface area, *i.e.* the amount of H_2 generation per surface area in terms of μmol h^{-1} m^{-2}.[30] Fig. S4† shows corresponding QE for orthorhombic and tetragonal $KNbO_3$ samples. The QE is 0.53 and 0.16% for o-$KNbO_3$ MCs and t-$KNbO_3$ MCs, respectively. This trend is in agreement with the observed photocatalytic activity as shown in Fig. 10. High quantum efficiency results from an increase in either the charge carrier lifetime or the interfacial electron-transfer rate constant, which is controlled by the electronic structure of $KNbO_3$ samples.[40] Table 1 lists the overall photocatalytic performance for orthorhombic and tetragonal $KNbO_3$ MCs and cubic $KNbO_3$ in the form of a cube-like morphology reported in previous work.[10] o-$KNbO_3$ MCs display a larger surface specific activity (234 μmol h^{-1} m^{-2}) than t-$KNbO_3$ MCs (173 μmol h^{-1} m^{-2}), while cubic $KNbO_3$ (c-$KNbO_3$) microcubes show the highest surface specific activity (318 μmol h^{-1} m^{-2}).

3.3 Theoretical calculations

In general, the photocatalytic reactivity of a photocatalyst is controlled by its structure and morphology such as particle size, crystal structure, and surface structure *etc*.[2,3] Both bulk and surface properties significantly impact the separation, mobility, and lifetime of the photogenerated electrons and holes, and often mediate the photocatalytic performance in a synergetic approach. Co-catalysts such as Pt deposited onto the photocatalyst surface can act as an electron trapping center under UV and are rather effective in inhibiting charge recombination. In the case of water splitting, photogenerated electrons that survive the electron–hole recombination can migrate to the photocatalyst surface to participate in the photocatalytic reaction. In this study, photocatalytic water splitting on cube-like $KNbO_3$ crystals was shown to be phase-dependent, with reactivities following the order cubic > orthorhombic > tetragonal. To shed light on the observed photocatalytic performance controlled by the crystalline phase and the associated bulk and electronic structure, we performed DFT calculations. The band gap of c-$KNbO_3$, o-$KNbO_3$ and t-$KNbO_3$ was calculated to be 1.55, 2.10, and 1.57 eV, while the experimental value is 3.24, 3.15, and 3.08 eV, respectively. The origin of this discrepancy lies in the use of DFT that generally underestimates the band gaps in semiconductors.[41] As shown in Fig. 11, all of the top valency bands are located at −5–0 eV, and the conduction bands are located at 1.5–16 eV. For example, for o-$KNbO_3$, the valence bands located around −10 and −27 eV are predominantly contributed by the K 3p and K 3s states, which are much more concentrated than those at −5eV to 0 eV. This behavior suggests that the electronic localization of this band is strong, the corresponding electrons have a large effective mass, and the electronic energy level is much lower than others. It is reasonable that it is difficult for the K atom to form a covalent bond with others. As shown in Fig. S5† there is no apparent overlap between the DOS of K and O, implying that the binding nature between K and O is ionic. The valence band of $KNbO_3$ is predominantly contributed by the O 2p and Nb 4d states, consistent with the XPS data shown in Fig. 5B. The DOS for the Nb 4d and O 2p states are similar from −5.5 to 0 eV, and there is hybridization between Nb 4d and O 2p. Further, the DOS of Nb 4d and O 2p demonstrates that the interplay between Nb and O is covalent.

As Ye *et al.*[31] pointed out, the higher symmetry in the crystal structure of cubic $NaNbO_3$ caused a much better photoreactivity than that of orthorhombic $NaNbO_3$. In the present work, O_h, C_{2v} and C_{4v} are the symmetries for the unit cell of c-$KNbO_3$, o-$KNbO_3$ and t-$KNbO_3$, respectively. Accordingly, the observed photocatalytic reactivity follows the order cubic > orthorhombic > tetragonal. Different from c-$KNbO_3$, the photogenerated electrons can not transfer isotropically in o-$KNbO_3$ and t-$KNbO_3$ (Fig. 12). Although the respective symmetry of the unit cell for o-$KNbO_3$ and t-$KNbO_3$ is C_{2v} and C_{4v}, the hydrogen production rate of o-$KNbO_3$ is more than that of t-$KNbO_3$. The lowest unoccupied wave functions (LUWFs) of the (110) and (001) planes for o-$KNbO_3$, and the (001) and (100) planes for t-$KNbO_3$ are shown in Fig. 13. It is notable that the spatial distributions of the LUWFs display a difference between o-$KNbO_3$ and t-$KNbO_3$. The LUMFs at (001) and (110) of o-$KNbO_3$ are mainly located at both the surface layer and subsurface layers. In contrast, the LUMF at (100) of t-$KNbO_3$ is located at the surface layer and the subsurface layers, while the LUMF at (001) of t-$KNbO_3$ is only located at the subsurface layers. Accordingly, photogenerated electrons should prefer to stay at the bottom of the o-$KNbO_3$ conduction band rather than that of t-$KNbO_3$. Because the surface photogenerated electrons are essential for the reduction reaction, o-$KNbO_3$ has a higher photoreactivity

than t-$KNbO_3$.[42] Our results not only emphasize the crucial role of the crystalline phase and the associated bulk electronic structure in heterogeneous photocatalysis, but also strongly suggest that tuning photocatalysts with particular facets allows the definition of photoreactivity as well.

4 Conclusions

Potassium niobate ($KNbO_3$) microcubes with orthorhombic and tetragonal phases were hydrothermally prepared. Compared to cubic $KNbO_3$ microcubes, the photocatalytic performance follows the order cubic > orthorhombic > tetragonal. First-principles density functional calculations shed new light on the origin of the observed phenomena. The best photocatalytic performance of cubic $KNbO_3$ is rationalized as the facile electron excitation and transfer dictated by it having the highest symmetry in the crystal structure and the resulting electronic structure in comparison with orthorhombic and tetragonal $KNbO_3$. Although the structural symmetry of orthorhombic $KNbO_3$ is lower than that of tetragonal $KNbO_3$, it presents a better performance due to the exposed facets and the associated electronic structure. The results of this work illustrate the effects of the crystalline phase and the associated electronic structure of perovskite-structured $KNbO_3$ and a range of perovskite-type mixed metal oxides on photocatalytic water splitting for hydrogen generation. In addition to water splitting, these results are potentially useful in other areas of heterogeneous photocatalysis, such as wastewater treatment, air purification, and fine chemical synthesis.

Acknowledgements

We gratefully acknowledge the financial support of this work from the National Natural Science Foundation of China (51272048, 20903099), Fundamental Research Funds for the Central Universities (N100605001) and 973 Program (2013CB632402). This work is also supported by the computing resources provided by the Supercomputing Center of the Chinese Academy of Sciences.

References

1 A. Fujishima and K. Honda, *Nature*, 1972, **238**, 37–38.
2 A. Kudo and Y. Miseki, *Chem. Soc. Rev.*, 2009, **38**, 253–278.
3 X. B. Chen, S. H. Shen, L. J. Guo and S. S. Mao, *Chem. Rev.*, 2010, **110**, 6503–6570.
4 X. M. Zhou, G. Liu, J. G. Yu and W. H. Fan, *J. Mater. Chem.*, 2012, **22**, 21337–21354.
5 Q. J. Xiang, J. G. Yu and M. Jaroniec, *Chem. Soc. Rev.*, 2012, **41**, 782–796.
6 J. G. Yu, B. Yang and B. Cheng, *Nanoscale*, 2012, **4**, 2670–2677.
7 Q. Li, B. Guo, J. Yu, J. Ran, B. Zhang, H. Yan and J. R. Gong, *J. Am. Chem. Soc.*, 2011, **133**, 10878–10884.
8 J. Zhang, J. Yu, Y. Zhang, Q. Li and J. R. Gong, *Nano Lett.*, 2011, **11**, 4774–4779.
9 Q. Xiang, J. Yu and M. Jaroniec, *J. Am. Chem. Soc.*, 2012, **134**, 6575–6578.
10 L. S. Yan, J. Zhang, X. M. Zhou, X. X. Wu, J. Y. Lan, Y. S. Wang, G. Liu, J. G. Yu and L. J. Zhi, *Int. J. Hydrogen Energy*, 2013, **38**, 3554–3561.
11 C. Z. Wen, Q. H. Hu, Y. N. Guo, X. Q. Gong, S. Z. Qiao and H. G. Yang, *Chem. Commun.*, 2011, **47**, 6138–6140.
12 T. K. Townsend, N. D. Browning and F. E. Osterloh, *ACS Nano*, 2012, **6**, 7420–7426.
13 H. Kato, K. Asakura and A. Kudo, *J. Am. Chem. Soc.*, 2003, **125**, 3082–3089.
14 H. Kato, H. Kobayashi and A. Kudo, *J. Phys. Chem. B*, 2002, **106**, 12441–12447.
15 M. A. Peña and J. L. G. Fierro, *Chem. Rev.*, 2001, **101**, 1981–2017.
16 J. W. Liu, G. Chen, Z. H. Li and Z. G. Zhang, *Int. J. Hydrogen Energy*, 2007, **32**, 2269–2272.
17 Q. P. Ding, Y. P. Yuan, X. Xiong, R. P. Li, H. B. Huang, Z. S. Li, T. Yu, Z. G. Zou and S. G. Yang, *J. Phys. Chem. C*, 2008, **112**, 18846–18848.
18 D. D'Elia, C. Beauger, J. F. Hochepied, A. Rigacci, M. H. Berger, N. Keller, V. K. Spitzer, Y. Suzuki, J. C. Valmalette, M. Benabdesselam and P. Achard, *Int. J. Hydrogen Energy*, 2011, **36**, 14360–14373.
19 T. R. Gordon, M. Cargnello, T. Paik, F. Mangolini, R. T. Weber, P. Fornasiero and C. B. Murray, *J. Am. Chem. Soc.*, 2012, **134**, 6751–6761.
20 X. M. Zhou, J. Y. Lan, G. Liu, K. Deng, Y. L. Yang, G. J. Nie, J. G. Yu and L. J. Zhi, *Angew. Chem., Int. Ed.*, 2012, **51**, 178–182.
21 Y. J. Chen, R. K. Huang, D. Q. Chen, Y. S. Wang, W. J. Liu, X. N. Li and Z. H. Li, *ACS Appl. Mater. Interfaces*, 2012, **4**, 2273–2279.
22 Y. K. Kho, A. Iwase, W. Y. Teoh, L. Mädler, A. Kudo and R. Amal, *J. Phys. Chem. C*, 2010, **114**, 2821–2829.
23 S. Tokunaga, H. Kato and A. Kudo, *Chem. Mater.*, 2001, **13**, 4624–4628.
24 Y. D. Hou, L. Wu, X. C. Wang, Z. X. Ding, Z. H. Li and X. Z. Fu, *J. Catal.*, 2007, **250**, 12–18.
25 Y. J. Chen, S. W. Hu, W. J. Liu, X. Y. Chen, L. Wu, X. X. Wang, P. Liu and Z. H. Li, *Dalton Trans.*, 2011, **40**, 2607–2613.
26 S. W. Liu, J. G. Yu and M. Jaroniec, *J. Am. Chem. Soc.*, 2010, **132**, 11914–11916.
27 C. Z. Wen, H. B. Jiang, S. Z. Qiao, H. G. Yang and G. Q. Lu, *J. Mater. Chem.*, 2011, **21**, 7052–7061.
28 J. Pan, G. Liu, G. Q. Lu and H. M. Cheng, *Angew. Chem., Int. Ed.*, 2011, **50**, 2133–2137.
29 H. G. Yang, G. Liu, S. Z. Qiao, C. H. Sun, Y. G. Jin, S. C. Smith, J. Zou, H. M. Cheng and G. Q. M. Lu, *J. Am. Chem. Soc.*, 2009, **131**, 4078–4083.
30 J. Zhang, Q. Xu, Z. Feng, M. Li and C. Li, *Angew. Chem., Int. Ed.*, 2008, **47**, 1766–1769.
31 P. Li, S. Ouyang, G. Xi, T. Kako and J. Ye, *J. Phys. Chem. C*, 2012, **116**, 7621–7628.
32 N. Kumada, T. Kyoda, Y. Yonesaki, T. Takei and N. Kinomura, *Mater. Res. Bull.*, 2007, **42**, 1856–1862.

33 M. D. Segall, P. J. D. Lindan, M. J. Probert, C. J. Pickard, P. J. Hasnip, S. J. Clark and M. C. Payne, *J. Phys.: Condens. Matter*, 2002, **14**, 2717–2744.
34 J. Y. Lan, X. M. Zhou, G. Liu, J. G. Yu, J. C. Zhang, L. J. Zhi and G. J. Nie, *Nanoscale*, 2011, **3**, 5161–5167.
35 K. Kakimoto, K. Akao, Y. P. Guo and H. Ohsato, *Jpn. J. Appl. Phys.*, 2005, **44**, 7064–7067.
36 X. M. Zhou, H. C. Yang, C. X. Wang, X. B. Mao, Y. S. Wang, Y. L. Yang and G. Liu, *J. Phys. Chem. C*, 2010, **114**, 17051–17061.
37 J. S. d. Andrade, A. G. Pinheiro, I. F. Vasconcelos, J. M. Sasaki, J. A. C. d. Paiva, M. A. Valente and A. S. B. Sombra, *J. Phys.: Condens. Matter*, 1999, **11**, 4451–4460.
38 A. V. Postnikov, B. Schneider, M. Neumann, D. Hartmann, H. Hesse, A. Moewes, E. Z. Kurmaev and M. Matteucci, *J. Phys. Chem. Solids*, 2000, **61**, 265–269.
39 L. G. C. Rego and V. S. Batista, *J. Am. Chem. Soc.*, 2003, **125**, 7989–7997.
40 M. R. Hoffmann, S. T. Martin, W. Y. Choi and D. W. Bahnemann, *Chem. Rev.*, 1995, **95**, 69–96.
41 R. Godby, M. Schlüter and L. Sham, *Phys. Rev. B*, 1987, **36**, 6497–6500.
42 Y. F. Li, Z. P. Liu, L. L. Liu and W. G. Gao, *J. Am. Chem. Soc.*, 2010, **132**, 13008–13015.